Understanding Frequency Response of a Flexural Complaint Stage for use in Oscillatory Orthogonal Cutting

by

Raul Barraza

Submitted to the
Department of Mechanical Engineering
in Partial Fulfillment of the Requirements for the Degree of

Bachelor of Science in Mechanical Engineering

at the

Massachusetts Institute of Technology

June 2015

Signature redacted

Signature of Author: _____
Department of Mechanical Engineering
May 26, 2015

Signature redacted

Certified by: _____
Martin L. Culpepper
Professor of Mechanical Engineering
Thesis Supervisor

Signature redacted

Accepted by: _____
Anette Hosoi
Professor of Mechanical Engineering
Undergraduate Officer

Understanding Frequency Response of a Flexural Complaint Stage for use in Oscillatory Orthogonal Cutting

by

Raul Barraza

Submitted to the Department of Mechanical Engineering
on May 26, 2015 in Partial Fulfillment of the
Requirements for the Degree of

Bachelor of Science in Mechanical Engineering

ABSTRACT

Ultramicrotomy is the process of cutting specimens into submicron-thickness slices for subsequent imaging using a scanning electron microscope (SEM). Ultramicrotomes, devices that employ this process, have incorporated oscillations into this process to reduce the damage done on each slice. Extensive research has been made in trying to identify the appropriate settings: frequency, amplitude of cut, and feed speed, to maximize the reduction of this damage. Currently, however, there exists no research that tries to understand why the introduction of oscillations provides such a reduction in damage. To understand the mechanics behind oscillatory orthogonal cutting, specifically in ultramicrotomy, the frequency response of a compliant mechanism must be understood. The frequency response of a complaint flexural stage driven by piezoelectric actuator was measured. Using a Linear Variable Differential Transformer (LVDT) and a dynamic signal analyzer via LabView, the frequency response of the stage was measured from $100Hz$ to $10000Hz$. A model was then fitted to the measured response. Using this model, a comparison between a simulated-reference response of the position of the stage to the output response of the model showed that a controller was required to minimize the error in the position of the stage.

Thesis Supervisor: Martin L. Culpepper
Title: Professor of Mechanical Engineering

Acknowledgement

I would like to thank Professor. David Trumper for providing me access to his lab and allowing access to all the equipment in the lab. I would like to thank Tyler Hamer for providing me with his dynamic signal analyzer, and for his help along this whole process. I would like to thank Mark Belanger at the Edgerton Student Shop for aiding me during use of the shop. Finally, I would like to thank Aaron Ramirez and Martin Culpepper for their guidance in this project.

Table of Contents

List of Figures

Chapter 1: Introduction

1.1 Introduction

The objective of this research is to understand the mechanics of oscillating orthogonal cutting in ultramicrotomy. Current research details an improvement in the surface quality and minimization in the damage of the sliced tissue when utilizing oscillating orthogonal cutting. However, there exists no literature detailing the mechanics behind oscillating orthogonal cutting. Understanding the mechanics behind these processes will enable engineers to reduce cutting forces and permanent surface deformation, while improving surface quality in the devices that implement ultramicrotomy, in order to successfully image brain samples volumes of 1 cubic cm. These improvements will become a stepping-stone to achieving a complete human brain map via serial sectioning. This research seeks to understand the dynamics of a compliant flexural stage that can be utilized in understanding the mechanics behind oscillatory cuts. This research lays the foundation in using compliant flexural stages in oscillatory cutting and provides the path for continued research into more complicated systems, as well as understanding the dynamics of such cuts.

1.2 Background

1.2.1 Introduction To Final Product

Figure 1, is a simple graphical representation of what this research sought to explore. A compliant flexural stage of mass, m, is oscillating at a frequency, f_o, and an amplitude, A. Utilizing a dynamic signal analyzer and test data, we sought to determine frequency response of the system, and how to utilize this response to design a flexural stage driven by a piezoelectric actuator that can be used to study the mechanics of oscillatory cuts. Once the frequency response was measured, a model was fitted to the response. A comparison between a simulated-reference

response for the position of the stage and the output response of the model showed that a controller is required in reducing the error of the system.

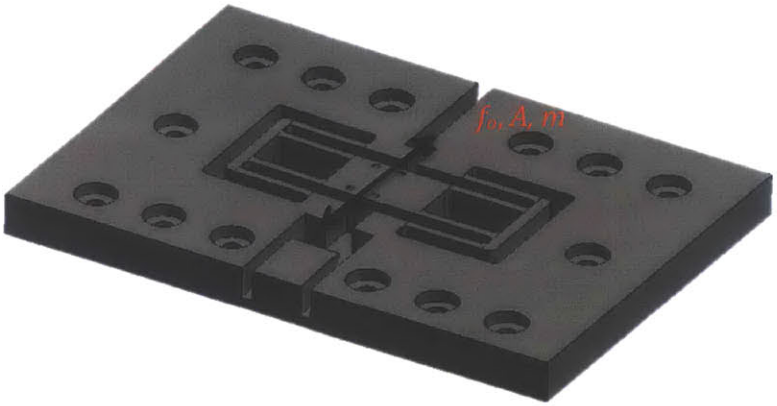

Figure 1: Drawing of the Device

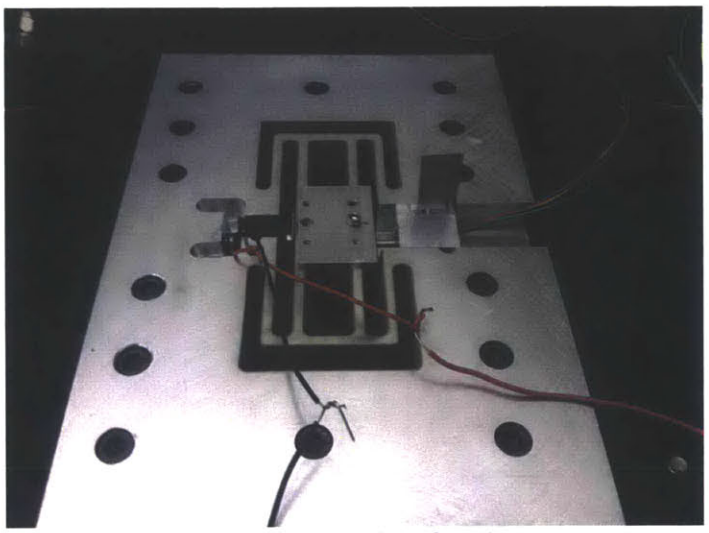

Figure 2: Image of Final Device

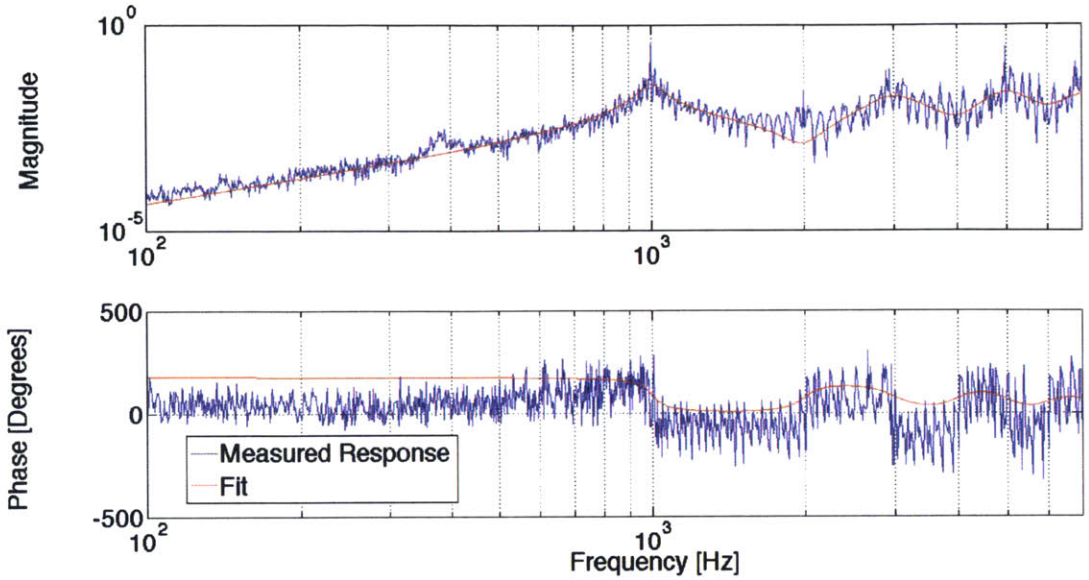

Figure 3:Measured Frequency Response with Fitted Model

1.2.2 Current Technology & Specific Motivation

Ultramicrotomy is the process of cutting specimens into submicron-thickness slices for subsequent imaging using a scanning electron microscope (SEM). Ultramicrotomy is schematically similar to orthogonal cutting, and the process of taking multiple cuts on an ultramicrotome in series is known as serial sectioning. After each layer is cut, the freshly cut block face is imaged in an SEM; this process is repeated until the entire specimen has been sliced and imaged. Each slice is then "stacked up," and reconstructed using software, giving a three-dimensional representation of the specimen and the interconnections between the neurons.

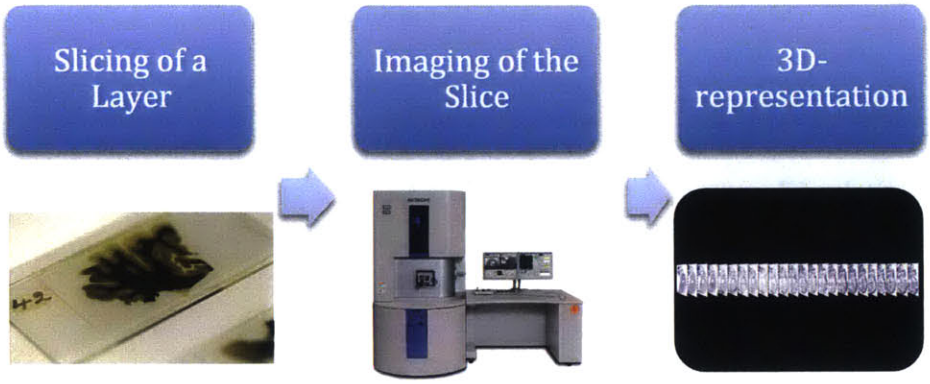

Figure 4: Process of Ultramicrotomy

Currently, commercial products such as the Gatan 3View use ultramicrotomy serial sectioning to image the neural paths within the brain for volumes as large as 0.01 mm^3. This machine implements an oscillating diamond blade to reduce the surface damage, cutting forces, and permanent deformation involved in the cutting process. Understanding, the mechanics behind oscillatory cuts can help in developing ultramicrotomes that are able to image volumes of brain larger than 0.01 mm^3, as well as higher quality slices. Such improvements could lead to breakthroughs in the understanding of the brain and as well as the diseases that afflict, which can result in new medical treatments that can aid the greater population.

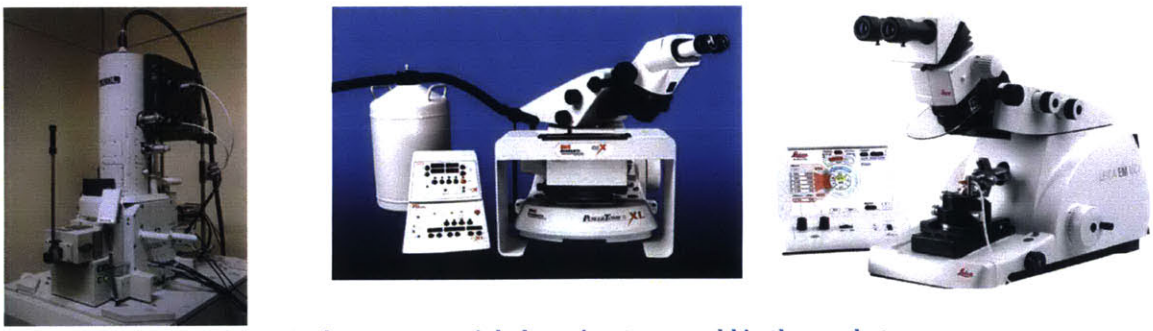

Figure 5: Three commercial ultramicrotomes sold in the market.

1.2.3 Larger Picture

Although the main motivation for understanding the mechanics behind such cutting process stems from trying to improve existing ultramicrotomes, this research has implication beyond this area. Oscillatory cutting process is not only used in slicing of brain samples in ultramicrotomy, but as well as in surgical tools in the medical field, and, metal cutting processes involved in several industries. Considering the medical field alone, various surgical tools, such as surgical bone saws, employ oscillatory cuts when being operated. Understanding the mechanics these cuts could lead to surgical tools that provide minimal damage to patient tissue during surgery, thus minimizing patient's recovery time, and saving millions of dollars in care and treatment.

Metal cutting processes are a large component in several manufacturing industries, including aeronautical, automotive, and electrical. With each of these industries outputting large volumes of products a day, small improvements in the metal cutting processes involved could lead to millions of dollars saved in energy consumption and material conserved. This research aims to give designers a new tool that aids in the design of devices that employ oscillatory cuts in order improve existing practices.

1.3 Prior Art

Very little work has been done in understanding the mechanics behind oscillatory cutting in ultramicrotomy. Most of the research involving such oscillatory cuts incorporates oscillations into ultramicrotomy to reduce the cutting artefacts in each slice: compression, crevasses and chatter. Compression is the shortening of the slice's length parallel to the cutting direction, resulting in an increase in the thickness of the slice with minimal change across the length perpendicular to the cutting direction. Crevasses are a system of fractures penetrating the slice from one side. Chatter is the periodic variation of the thickness of the slice along the cutting

direction[1]. These cutting artefacts create inconsistencies in the tissue slices that diminish the accuracy provided by the 3D representation of the scanned tissue samples. According to the research done by Daniel Studer, Ashraf Al-Amoudi, and Kasim Sader, incorporating oscillations varying from $2kHz$-$40kHz$ with a stroke of $20nm - 400nm$ minimizes any chatter and crevasses[1] seen in the slice, and reduces compression by 15%[2]. In addition, research headed by Hongyan Gu characterized the complete removal of chatter when cutting at a frequency higher than 25 kHz and a cutting speed of greater than 0.2 mm/s (cutting speed is the velocity at which the sample was feed into the oscillating blade)[3]. In most biological practices, the understanding of the mechanics behind oscillatory cuts is not critical as long as the improvements are seen during the process of ultramicrotomy. This could explain the limited amount of research in trying to understand oscillatory cutting processes.

Chapter 2: Fundamentals of Oscillatory Oblique Cutting

2.1 Orthogonal Cutting

Simple orthogonal cutting is a metal cutting process representative of the cutting mechanics in many machining operations, such as turning, planing, and facing. In orthogonal cutting, as metal approaches the edge of the tool, it deforms by shear. As the material shears, it plastically deforms, creating chips that flow up the orthogonal plane, the face of the tool[4]. Given the good approximation of orthogonal cutting for the major cutting edges in many machining operations, several models have been created in order to understand the mechanics behind this cutting process. Each of these models is an idealized case for the cutting process in orthogonal cutting, and each holds its own limitations.

2.2 Merchant's Model

Merchant's model is an idealized model of the orthogonal cutting that represents the formation of chips through the concentration of a shearing process across the primary shearing plane. In this model, the material is considered to be homogenous via the following assumptions[4]:

1. The tool is perfectly sharp and there is no contact along the clearance face.
2. The shear surface is a plane extending upward from the cutting edge by and angle, ϕ.
3. The cutting edge is a straight line extending orthogonal to the direction of motion and generates a plane surface as the work moves past it.
4. The chip does not flow to either side (i.e. plane strain).
5. The depth of cut is constant.
6. The width of the tool is greater than that of the workpiece.
7. The work moves relative to the tool with uniform velocity.
8. A continuous chip is produced with no built-up edge.
9. The shear and normal stresses along shear plane and tool are uniform.

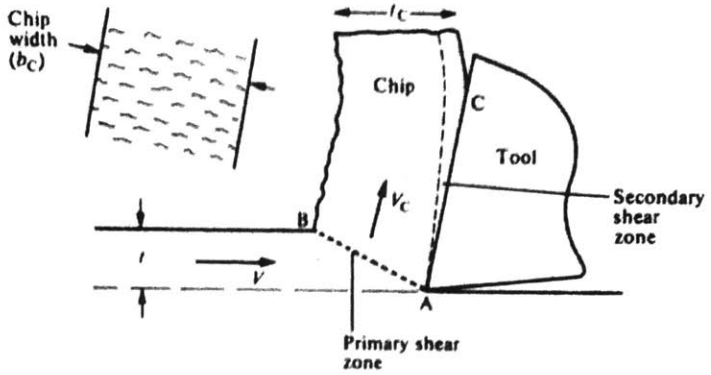

Figure 6: Figure of merchant's model for orthogonal cutting with primary shear plane, tool, and chip[4]

The model, however, fails when the workpiece is soft and not prestrain hardened before cutting, or when the radius of the tool is of significant size relative to the undeformed chip thickness. In these two cases, the shear plane becomes either a pie-shaped zone or an undefined shear zone[4].

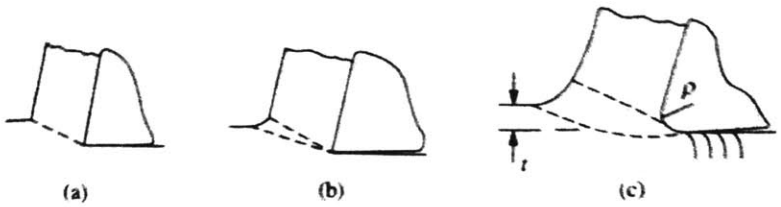

Figure 7: Graphical Representation of the three primary shear zones experienced in metal cutting. A) Merchant's model for the primary shear plane. B) Pie-shaped shear zone seen when cutting soft and prestrained materials. C) Undefined shear zone seen in metal cutting when tool has radius that significantly large relative to depth of cut[4].

2.2.1 Shear

In Merchant's model, the primary shear plane is defined by the shear angle, ϕ, which is the angle from the straight line extending from the cutting edge. This angle can be defined using the cutting ratio, r, the ratio of the depth of cut, t, to the chip thickness, t_c. Given that there is no change in the density of the material when cut, the volume of the undeformed chip equals the volume of the chip. Thus, the cutting ratio can be defined as follows:

$$r = \frac{t}{t_c} \quad [1]$$

This is assuming that the ratio of the width of cut and the depth of cut, t, are greater than or equal to five. By looking at the geometric relationships between the workpiece, the chip, and the primary shear plane, the relationship between the cutting ratio and the shear angle is defined as follows:

$$r = \frac{ABsin\phi}{ABcos(\phi-\alpha)} \quad [2]$$

Thus, the shear angle can be defined as follows:

$$tan\phi = \frac{rcos\alpha}{1-rsin\alpha} \quad [3]$$

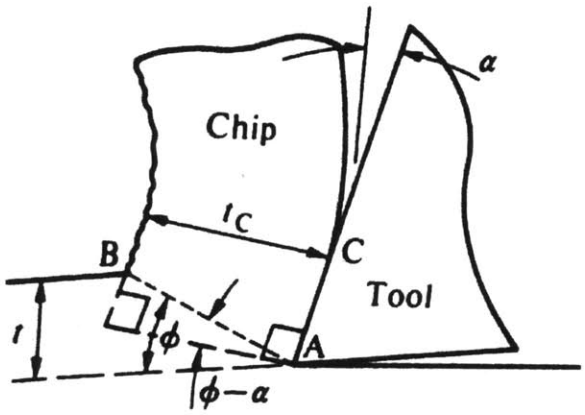

Figure 8: Pictorial Representation of the geometric relationship between shear angle and the cutting ratio. α is the rake angle, the angle from the tool face to the normal from the workpiece[4].

At the primary shear plane, the shear strain, γ, experienced by the workpiece is defined by ratio of the infinitesimal shear over the infinitesimal section of material of height Y.

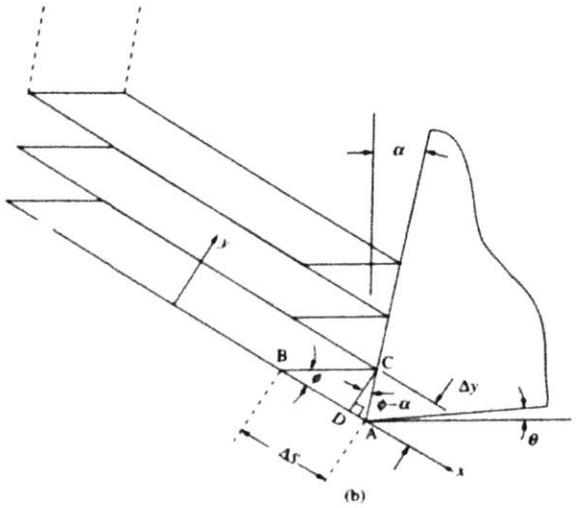

Figure 9: Pictorial representation of the shear strain that occurs in orthogonal cutting[4].

Given the geometric relationships between the sheared infinitesimal piece of material at the primary shear plane and tool point shown in Figure 7, the shear strain becomes:

$$\gamma = \frac{\Delta s}{\Delta y} = \tan(\phi - \alpha) + cot\phi \qquad [4]$$

Where the α is the rake angle, ϕ is the shear angle, and Δy is the thickness of the shear zone.

2.2.2 Forces & Stresses

Two forces are present during orthogonal cutting: a force, R, at the interface between the tool face and the chip, and a force, R', at the interface between the workpiece and the chip along the shear plane. These forces can be broken down into a set of three components acting along the x and y directions (F_p and F_Q, respectively), as well as normal and perpendicular to the two interfaces of the chip (F_S and F_C respectively). Translating these forces to the point of the tool, the composite cutting force circle is created where the R is the diameter of the circle. Thus, the shear and friction forces, and the coefficient of friction at the two interfaces of the chip can be defined as functions of the geometric relationships of the this diagram, and F_P and F_Q.

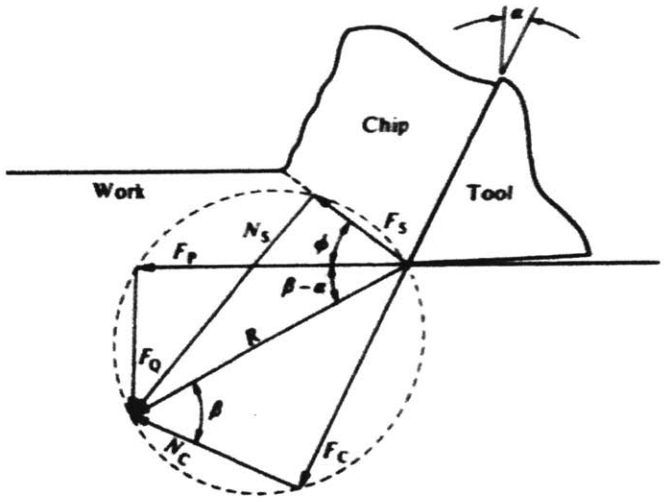

Figure 10: Merchant's Composite Circle[4].

Given this, the mean shear and normal stresses on the shear plane can be defined as functions of the same geometric values and the forces from the composite cutting circle in Figure 8. Thus, the mean shear stress and the normal stress can be defined as follows, where A_s is the area of the shear plane:

$$A_s = \frac{bt}{sin\phi} \quad [5]$$

$$\tau = \frac{F_s}{A_s} = \frac{(F_p cos\phi - F_Q sin\phi)sin\phi}{bt} \quad [6]$$

$$\sigma = \frac{N_s}{A_s} = \frac{(F_p cos\phi + F_Q sin\phi)sin\phi}{bt} \quad [7]$$

2.2.3 Velocity Relations

In orthogonal cutting there are three velocities of importance: the velocity of the tool relative to the work, V, the velocity of the chip relative to the tool, V_C, and the velocity of the chip relative to the workpiece along the shear plane, V_S. When considering the kinematic principles of the chip, these three velocities form a closed velocity diagram, shown in Figure 9.

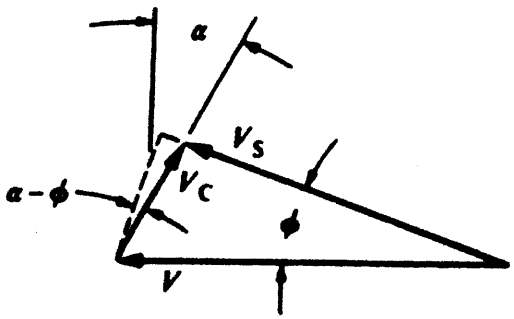

Figure 11: Pictorial Representation of the velocity diagram[4].

From the geometric relationship between these three velocities, the chip velocity and the shear velocity are defined as follows:

$$V_c = \frac{sin\phi}{\cos(\phi - \alpha)} V \quad [8]$$

$$V_s = \frac{cos\alpha}{\cos(\phi-\alpha)}V \quad [9]$$

2.2.4 Strain Rate

Using these three velocities, the strain rate can be defined as the ratio of shear per thickness of the shear zone per unit time along the shear plane, which is equivalent to the ratio of the shear velocity per unit thickness of the shear zone.

$$\dot{\gamma} = \frac{\Delta s}{\Delta y \Delta t} = \frac{V_s}{\Delta y} \quad [10]$$

By substituting equation 9 into the equation above, the strain rate is defined by the shear angle, the rake angle, and the velocity, V, and the thickness of the shear zone.

2.2.5 Energy Approach

In orthogonal cutting, the energy consumed per unit time is defined by the product of F_P and the velocity, V.

$$U = F_p V \quad [11]$$

Dividing this total energy by the velocity, V, the depth of cut, b, and the width of cut, t, the total energy per unit volume of metal removed, otherwise known as the specific energy, u, can be defined as follows:

$$u = \frac{U}{Vbt} = \frac{F_p}{bt} \quad [12]$$

The specific energy is an intensive value that quantifies the resistance of the material during the cutting process. Most of this energy is consumed along the primary shear plane and the tool face.

$$u = u_s + u_F \quad [13]$$

The shear energy per unit volume is defined as follows:

$$u_s = \frac{F_s V_s}{Vbt} = \tau \frac{V_s}{Vsin\phi} \quad [14]$$

The energy expended via friction per unit volume is defined as follows:

$$u_F = \frac{F_c V_c}{Vbt} \qquad [15]$$

2.3 Oblique Cutting

Oblique cutting is a variation of orthogonal cutting in which the cutting edge of the tool is at some angle, i (inclination angle), from the direction of motion of the workpiece. This form of cutting models the mechanics in cutting processes involving scissors, oscillating blades, and scythes. In oblique cutting, the slice-push ratio, ξ, a ratio of the blade displacement to the displacement of the workpiece, is a critical parameter in minimizing the cutting forces involved in such cuts. The slice-push ratio is obtained via the following: a) an orthogonal blade driven sideways and down, b) when a blade is driven down workpiece at an inclination angle, c) when the blade is driven down the workpiece at an inclination angle while moving in the same direction parallel to the cutting edge[5].

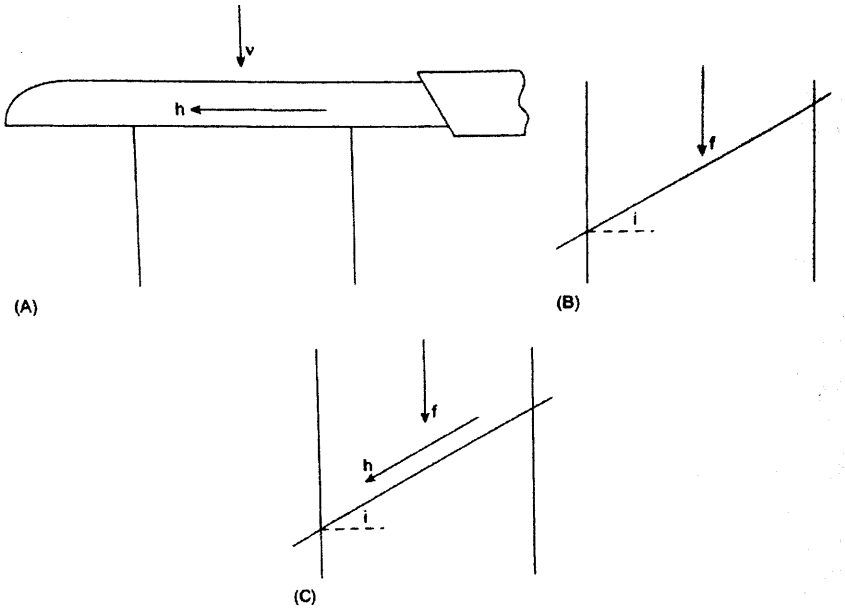

Figure 12: Three situation of oblique cutting from which the slice-push ratio exists[5]

2.3.1 Cutting Forces

Focusing on case a in Figure 11, a blade of angle, θ, experiences two displacements, a movement, *dh*, parallel to the cutting edge and a displacement, *dv*, perpendicular to the blades cutting edge.

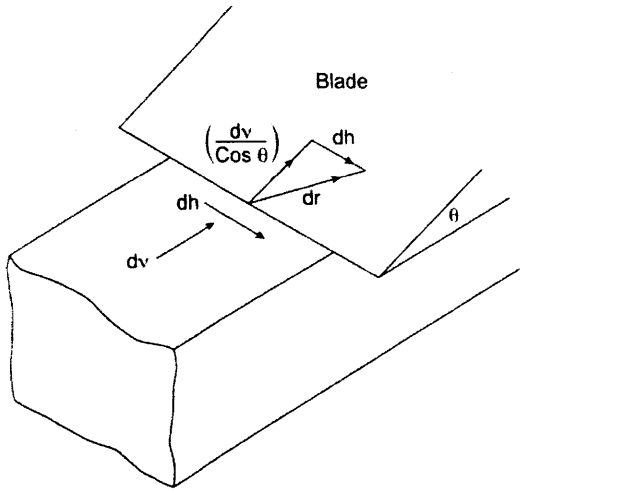

Figure 13: Pictorial representation of the displacements seen in an orthogonal blade moving parallel and normal to the cutting edge of the blade[5].

The resultant displacement of the offcut over the face of the tool can be defined using the geometric relationships in Figure 11. Since the slice-push ratio is defined as the ratio of these two displacements, the resultant displacement can be written using the slice-push ratio.

$$dr = \sqrt{(dh)^2 + \left(\frac{dv}{cos\theta}\right)^2} = \frac{dv}{cos\theta}\sqrt{(\xi cos\theta)^2 + 1} \qquad [16]$$

In oblique cutting, the two forces involved are F_V and H, and act parallel to the *dv* and *dh*, respectively. During this cutting process, the work done for each increment of movement is defined as the sum of the work expended in both directions of motion:

$$W = Vdv + Hdh \quad [17]$$

This incremental work is the amount of work required via fracture, which is defined as $Rwdv$, where R is the specific work for surface separation of the material and w is the width of the cut. As a result, the incremental work can be redefined as follows:

$$W = Vdv + Hdh = Rwdv \quad [18]$$

When looking at the interface between the chip and the tool, the resultant force of friction is acting in the same direction as the resultant displacement. Thus, the frictional work expended for each displacement dr, is as follows, where μ is the coefficient of friction and N is the normal force acting on the tool face:

$$W_f = \mu N dr \quad [19]$$

By substituting for dr and N, the force normal to the cutting edge, the incremental frictional work is redefined as follows:

$$W_f = \frac{\mu V\sqrt{(\xi cos\theta)^2+1}dv}{cos\theta(sin\theta+\mu cos\theta)} \quad [20]$$

In equating the external and internal incremental works, the forces, F_V and H are defined as follows:

$$\frac{F_V}{Rw} = \frac{1}{(1+\xi^2-(2\mu\sqrt{(\xi cos\theta)^2+\frac{1}{(cos\theta(sin\theta+\mu sin\theta))}}} \quad [21]$$

$$\frac{H}{Rw} = \frac{\xi F_V}{Rw} \quad [22]$$

2.3.2 Reciprocating Blades

When dealing with reciprocating blades, the oscillations are defined as follows:

$$h = Asin(\omega t) \tag{23}$$

During the reciprocation of the blade, as the workpiece is being feed to the tool, the slice-push ratio changes in value. At the end of each oscillation the slice-push ratio become zero as the blades comes to rest, and reaches a maximum value during the middle of the stroke. As result the forces F_V and H become dependent on the oscillation of the blade. With this in mind the, slice-push ratio, and the forces F_V and H can defined as follows:

$$\xi = \frac{h}{v} = \frac{A}{v} sin\omega t \tag{24}$$

$$\frac{F_V}{Rw} = \frac{1}{(1+(\frac{A}{v}sin\omega t)^2-(2\mu\sqrt{\left(\frac{A}{v}sin\omega t cos\theta\right)^2+\frac{1}{(cos\theta(sin\theta+\mu sin\theta))}}} \tag{25}$$

$$\frac{H}{Rw} = \frac{F_V}{Rw}\left(\frac{A}{v} sin\omega t\right) \tag{26}$$

Chapter 3: Compliant Structures

Compliant structures are a wide subset of mechanical systems that utilize the elasticity of systems to actuate systems small displacements via an applied force. A compliant flexural mechanism is a single-pieced structure that incorporates flexures to provide motion in the desired directions, while providing constraints in all others. These types of systems are favorable in precision engineering because they allow for frictionless-movement for a controlled and limited range. These systems can be found in many several systems, including atomic force microscopes and optical equipment, and are a big area of interest in precision engineering[6].

3.1 Compliant Flexural Systems

Compliant flexural systems utilize the elastic deformation in beam bending to provide the desired motions. These systems are comprised of four components, an actuator the compliant stage, the flexures, and ground, as seen in Figure 13.[7]

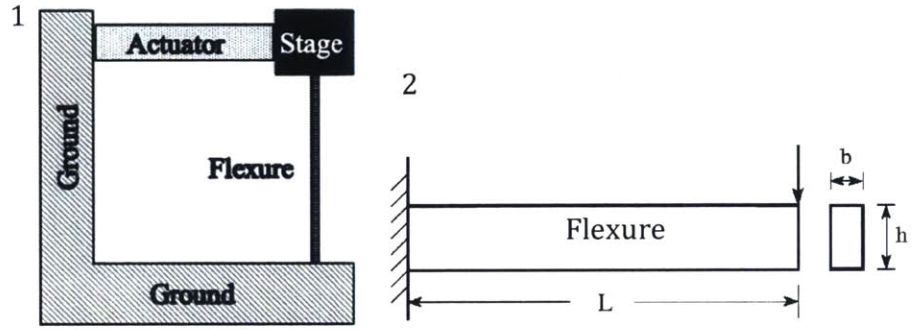

Figure 14: 1) Pictorial Representation of the four components that comprise a complaint structure. 2) Cantilevered Beam used to model flexure deflection[7].

Ground is the portion of the system that is fixed to the rest of the system by means of an attachment mechanism, rivets, bolts, etc. This component of the mechanism should not experience any movement with respect to the stage. The stage is the component of the system that desired object is secured. The flexures are the elastic beams of the system that deflect when

a force is applied in the desired direction, but restrict motion in all others. The actuator is the device that provides the force.

To understand the relationship between the deflection of the system and the force applied, the entire system can be simplified to a mass attached to a spring connected to ground, as seen in Figure 14.

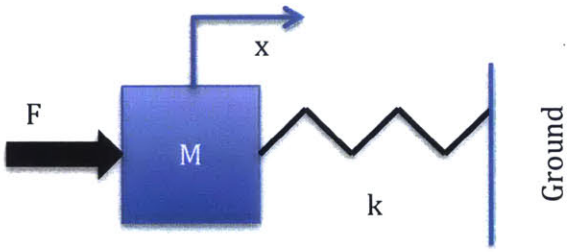

Figure 15: Mass-Spring model used to model complaint flexural structures.

The spring represents the deflection of the flexure and the mass is the mass of the stage and the desired object. When the actuator applies the force, the mass will move some displacement dependent on the stiffness of the spring, k. Assuming a Newtonian spring, there is a positive correlation between the force and the displacement, as seen by the following:

$$F = k\delta \qquad [27]$$

To find the stiffness of the idealized spring, the bending experienced the flexure must be characterized. In this simple model, the flexure of Figure 13 is a cantilevered beam grounded at one end and free to move at the other. Assuming a rectangular cross sectional area, the deflection at the tip of the flexure is given by the following[8]:

$$\delta = \frac{FL^3}{3EI} \quad [28]$$

$$I = \frac{bh^3}{12} \quad [29]$$

E is the young's modulus of the material the flexure is composed of. The stiffness of the flexure can be derived by rearranging δ:

$$k = \frac{3EI}{L^3} \quad [30]$$

All compliant flexural systems can be simplified into a mass and spring model. The math however, will vary depending on the complexity of the system.

3.2 Piezoelectric Actuators

When utilizing compliant flexural systems, the selection of the actuator is a critical step in the design of the system. For small-scale systems, due to limitations in space, a small actuator that can provide sufficient force to move stiff stages is required. Piezoelectric actuators are often the choice of actuators for such systems. There are several types of piezoelectric actuators, including stacks, plates, or benders, as shown in Figure 15.

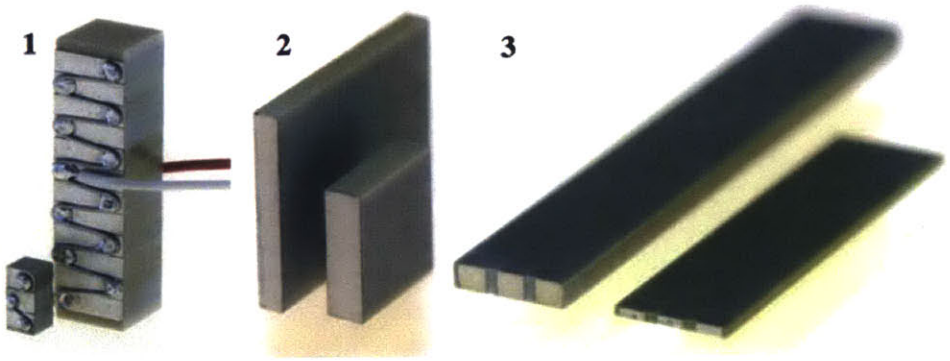

Figure 16: Different Piezoelectric actuators available in the market. 1) Stacked Piezoelectric actuator. 2) Plate Piezoelectric Actuator. 3) Bender Piezoelectric Actuator[7].

When an electric field is applied to the material of the actuator, the actuator experiences a displacement and a force along with it. Focusing on a stacked piezoelectric actuator, the blocking force produced by such an actuator is positively correlated to the displacement the actuator experiences and is defined as follows[9]:

$$F_{block} = k_p \Delta L \quad [31]$$

ΔL, is the change in the length of the piezoelectric actuator and k_p, is the stiffness of the actuator itself, and is defined as follows:

$$k_p = \frac{AE}{L} \quad [32]$$

$$A = wt \quad [33]$$

E is the young's modulus of the material the actuator is made out of and, w, L, and t are all geometric properties of the system itself, as shown in Figure 16.

Figure 17: Diagram of Stacked Piezoelectric Actuator Geometry[7].

Chapter 4: Assessment of Design and Theory

4.1 Vibrating Flexural Stage Design

4.1.1 Design Specifications

A flexural stage that oscillated at a frequency, f_o, and an amplitude, A, was explored as a possible design to incorporate oscillations in ultramicrotomes. In order for the stage to run properly it needed to adhere to the requirements in Table 4.1.

Table 1: Comparison of the Desire design specifications to the actual design specifications.

Requirements	Desired	Actual
Amplitude	+/- 5 microns	+/- 5 microns
Driving Frequency	1000-2000 Hz	1000-2000 Hz
Stiffness in Y	154 N/micron	63.7 N/micron
Stiffness in Z	21.5 N/micron	16.5 N/micron
Natural Frequency	>2000 Hz	5270 Hz

4.1.2 Linear Stage Design

To arrive to the optimal flexural design, FACT was implemented. By defining the freedom space as a single line and the constraint space as five planes normal to the freedom space, the following two concepts were conceived[10].

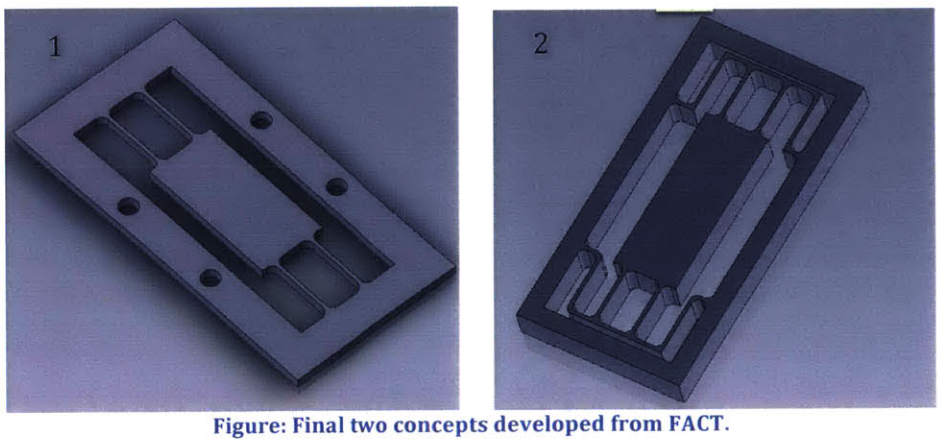

Figure: Final two concepts developed from FACT.

Concept 2 was chosen as it was found to provide the same stiffness for a smaller flexure length, implying an overall smaller stage. This is desirable, as it allows for easier implementation of such a design in actual microtomes where space is limited. Concept 2 consisted of a set of four parallel flexures, parallel to each other. The flexure geometries will all be the same, resulting in all eight flexures having the same stiffness. When modeling the design as a mass-spring model, the mass is attached to two sets of parallel springs on each side of the mass. Each of the parallel spring contains two springs in series.

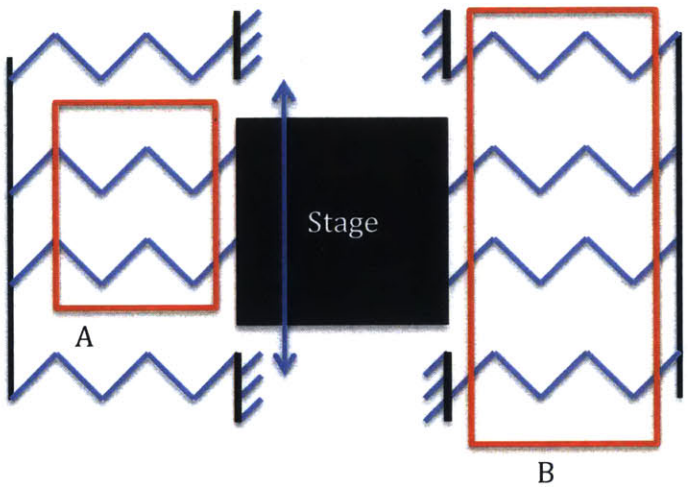

Figure 18: Mass-spring model of concept 2 design.

The overall stiffness of the spring was found to be:

$$k_a = k_b = k + k \quad [34]$$

$$\frac{1}{k_1} = \frac{1}{k_a} + \frac{1}{k_b} \quad \& \quad \frac{1}{k_2} = \frac{1}{k_a} + \frac{1}{k_b} \quad [35]$$

$$K_{eq} = k_1 + k_2 \quad [36]$$

Given that all eight flexures have the same stiffness, the overall stiffness of the flexure is *2k*.

4.1.3 Characterization of Actuator Performance

A stacked piezoelectric actuator was chosen to actuate the stage as it has a low enough slew time to operate at given drive frequency and can provide the desired amplitude range. The specific stacked piezoelectric actuator chosen was the TS18-H5-104 actuator from Piezo Systems, Inc. This actuator provides 14.5 microns of free deflection and a blocking force of 840 *N*. For the stage to be driven a total of ten microns, the force that the actuator produces at such a displacement needs to be known[11]. From Figure 19, the force at a 10-micron displacement ranges from 172-345 *N*. However, with actuator experiencing displacement variations of 1 micron, the minimum force produced for a 9-micron deflection is used throughout the design of the stage. This force is 119 *N*.

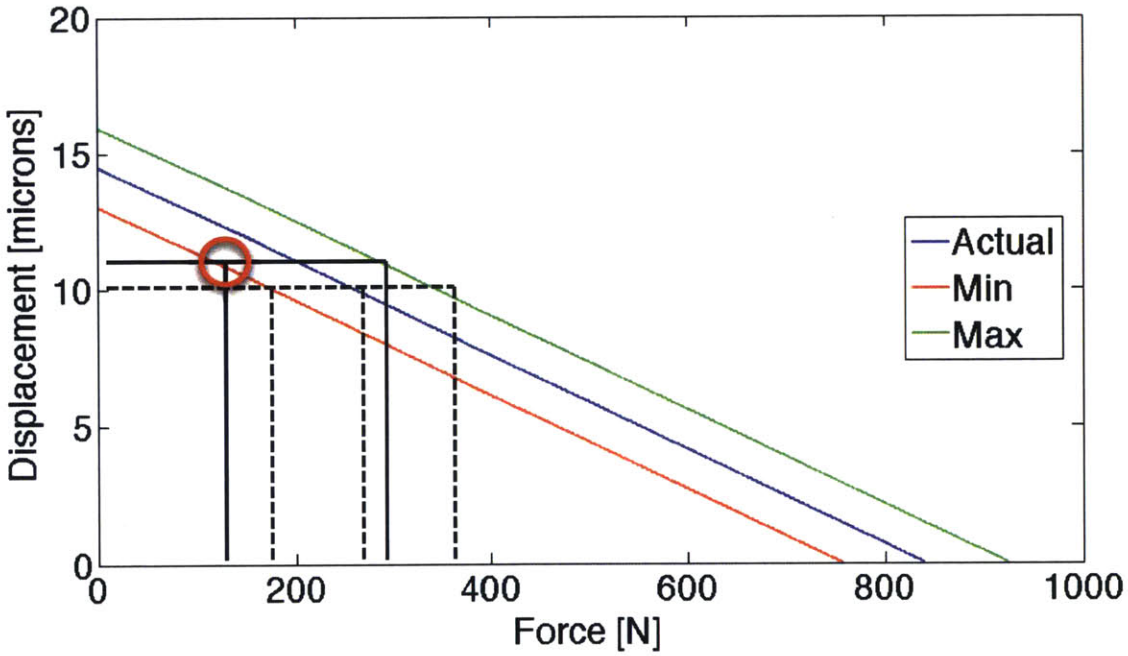

Figure 19: Actuator Performance

4.1.4 Dynamic Design

Literature has shown that a frequency range of 2000*Hz* -20000*Hz* improved the quality of slices in ultramicrotomy. Thus, a maximum range of 2000*Hz* was chosen as it is within the aforementioned range, yet was feasible to design around given the limitations of the piezoelectric actuator. At 2000*Hz*, the actuator is able to respond to the voltage at which it is being driven. The stiffness of the stage must be chosen such that the flexure can respond at the desired frequency when driven by the actuator. Simplifying the flexural stage into a mass-spring model, as shown in Figure 20, the dynamics of the mass can characterized using Newton's Second law and Hooke's Law. The damping was ignored, as the damping found within most metals is negligible.

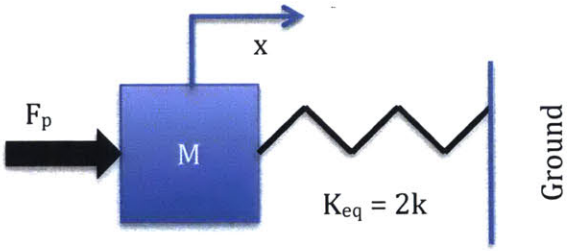

Figure 20: Simplified mass-spring model of concept 2.

$$\Sigma F = ma \text{ and } F_k = kx \quad [37]$$

$$F_p - F_k = ma \quad [38]$$

$$F_p = m\ddot{x} + kx \quad [39]$$

Given that this is the second order differential equation for an un-damped system, the position of this equation becomes:

$$x(t) = Acos(\omega t) \text{ where } \omega = \sqrt{\frac{k}{m}} \quad [40]$$

With the amplitude, A, being 10 microns, and the frequency, ω, being $2000Hz$, for a single oscillation the position, *x (at t =0.0005s),* of the stage will be 0 microns. The mass of the stage, *m,* is 0.0569 *kg*. Thus, k can be found by moving around the solution as follows:

$$k = m\left(\frac{\pi}{2t}\right)^2 \quad [41]$$

Plugging in these values gives a stiffness of $0.5N/$micron. With this stiffness being two orders of magnitude lower than the maximum stiffness of the actuator ($\sim 80N/$micron), the output force of the actuator will be used in determining stiffness of the flexure.

For a 10-micron displacement, the output point force used is $119N$. For the stage to operate within the given design requirements, the stiffness must be within 0.5-$80N/$micron. In operating the stage at the desired amplitude, a 10-micron offset is required. As such, the stiffness of the stage must not be such that piezoelectric actuator is unable to provide sufficient force to displace the stage an additional 10 microns. The stiffness, however, cannot be so low that unforeseen errors via machining/installation will cause the stiffness to be below the minimum threshold of $0.5N/$microns. Thus, a stiffness of $5N/$microns was chosen, as it provided a force of 50 N onto the stage, while still being 10 times larger than the minimum threshold accounting for any errors that might occur.

4.1.5: Flexural Stage Design

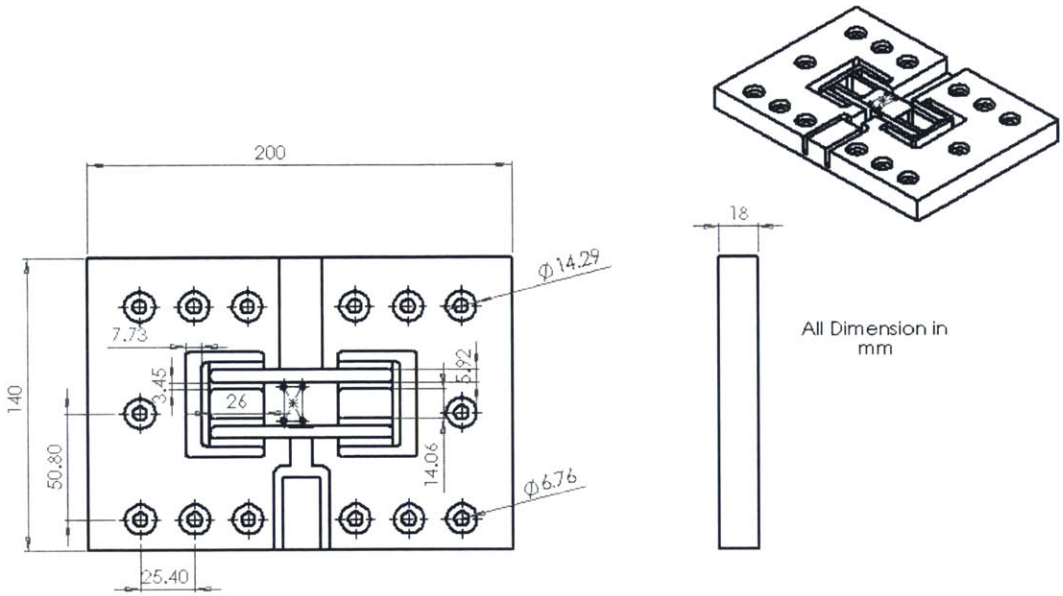

Figure 21: Final Design of Stage Design Values presented are valued measured post-fabrication

Figure 21, shows the final stage design with the critical part features labeled. The exact stiffness ($\sim$4.69 N/micron) of the system was determined via finite element analysis. Slots where machined into the sides of the stage to allow for installation of a sensor and actuator.

4.1.6: Actuator Connection

Installation of the actuator required that the actuator experienced no shear during operation of the stage, as any shear would cause the PZT material fail. As a result, rounded ends were attached to the end of the actuator to ensure that if any shear were to occur the ballpoint contact would allow rolling at the intersection. For the stage to operate within the required specifications, it was determined that a 10-micron offset with a stiffness of 5N/micron was required. To introduce the 10-micron offset into the system, steel plates are introduced at both ends of the actuator. Since the rounded tips introduce Hertzian deformation, it is important to characterize such deformation. For a ball-to-plate contact the Hertzian deformation is defined as follows:

$$\delta = \left(\frac{9F^2}{32R_eE_e}\right)^{\frac{1}{3}} \quad [42]$$

where $E_e = 106\,GPa$ & $R_e = 1000\,mm$

With a 10-micron offset and a stiffness of 5 N/micron, the maximum force required by the actuator during one oscillation is 100 N. Thus, a maximum 6.78 microns of Hertzian deformation is expected to occur. Figure 22, is a pictorial representation of the actuator assembly.

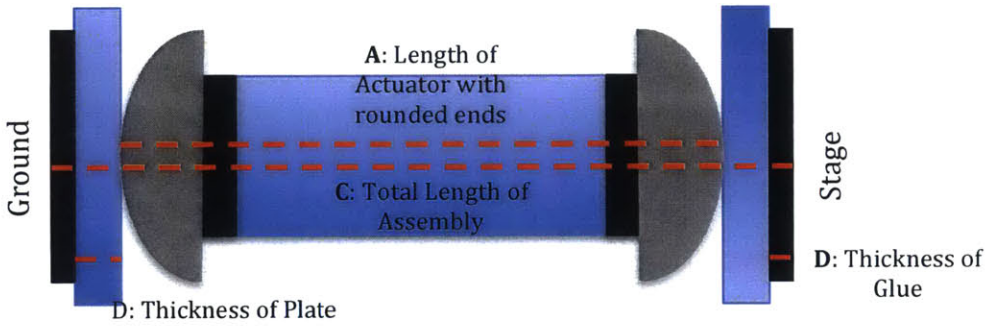

Figure 22: Pictorial Representation of Actuator Assembly.

In determining the thickness of the steel plates, the following variables in Figure 22, along with the Hertzian deformation were used. The thickness of the bonding agent was used experimentally to be 79 microns. Compression experienced by the bonding agent was neglected as the molecular composition of the epoxy prevents the material from compressing for small thicknesses; these results were verified experimentally as well. Thus, the following relationship was determined:

$$C + 0.01mm = A + 2B + 2D - 2\delta_{Hertz} \quad [42]$$

Solving for D, the plate thickness required was 0.989 *mm*. Figure 23, shows the final assembled actuator.

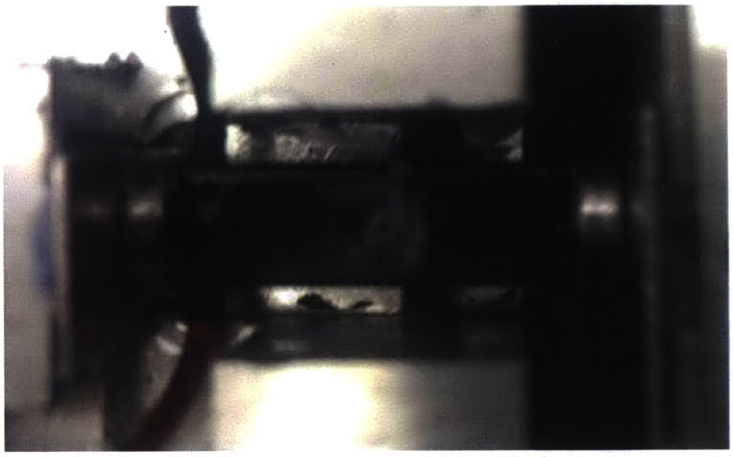

Figure 22: Final assembled actuator installed into stage.

4.2 Dynamic Behavior

With a final stage design at hand, the electromechanical system was modeled as shown in Figure 23. The force, F_p, is proportionally related to the voltage, *e,* applied to the actuator via a constant K_p.

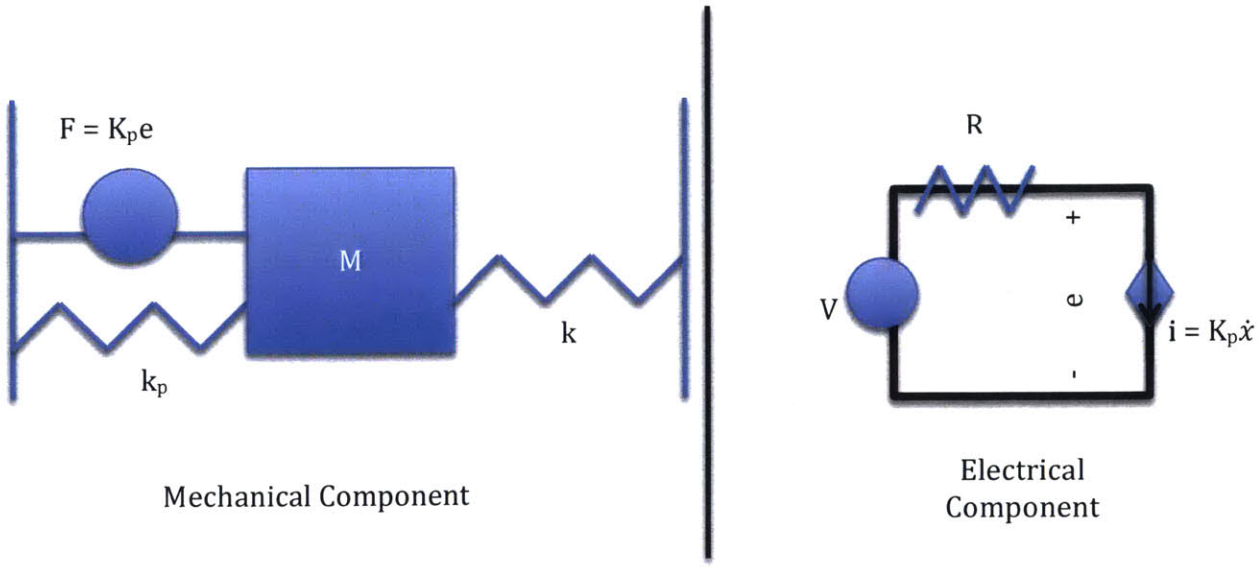

Figure 23: Simplified Model of the Electromechanical system

Using Hooke's Law and Newton's second law, the position of the mass, can be characterized as follows:

$$\Sigma F = ma \quad [43]$$

$$F_k = kx \quad [44]$$

$$F_p - F_k - F_{piezo} = ma \quad [45]$$

$$F_p = m\ddot{x} + (k + k_p)x \quad [46]$$

Given the relationship of the actuator force to the voltage, *e*, the force of the actuator can be defined as follows:

$$F_p = K_p(V - K_p R\dot{x}) \quad [47]$$

Plugging this relationship into the differential equation for the un-damped second order system becomes a damped, as shown:

$$K_p V = m\ddot{x} + K_p^2 R\dot{x} + (k + k_p)x \quad [48]$$

$$\text{where } \omega_n = \sqrt{\frac{k+k_p}{m}} \ \& \ \xi = \frac{K_p^2 R}{2m\omega_n} \quad [49]\ [50]$$

With K_p = 6.67 N/V (from manufacture), R = 100 ohms, k = 5N/micron, k_p = 80 N/micron, and m = 56.9 g, the expected frequency of the system is that of damped second order system, with resonance approximately at the natural frequency, indicated by the peak on the magnitude plot and phase drop of 180 degrees at the natural frequency. This response is shown in Figure 24.

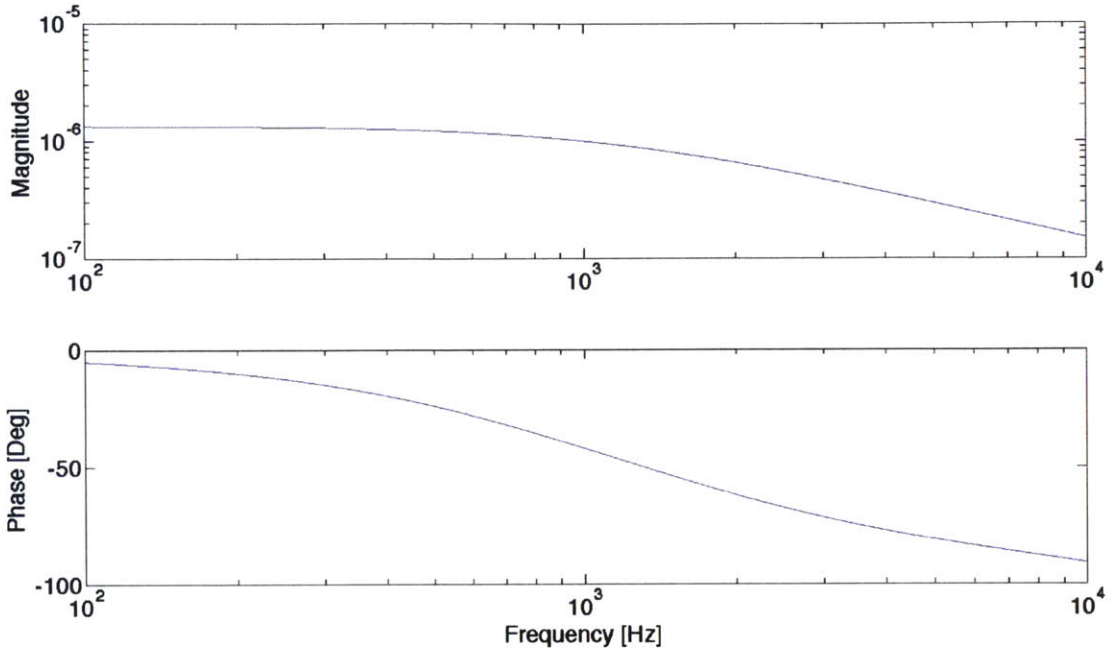

Figure 24: Expected frequency response of system

Chapter 5: Validation of Design

5.1 Instrumentation and Setup

In order to measure the frequency response of the system, an MHR 025 Linear Variable Differential Transformer (LVDT) with a Schaevitz ATA 2001 LVDT signal conditioner is used to measure the position of the stage during operation. To properly measure the response, the signal conditioner was calibrated via calibration setup consisting of Thorlab 25mm stage, LVDT holder, and a core couple. Figure 25, shows the assembled calibration setup.

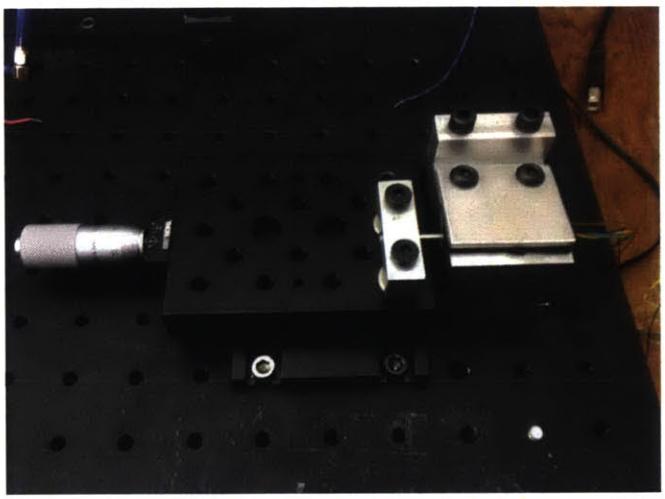

Figure 25: Assembled Calibration Setup

A calibration constant was measured by sweeping through a core displace of +/- 100 microns, and recording the output voltage. The output voltage was then plotted against the core displacement. A line of best fit was applied to the data, in order to obtain the calibration constant (slope of the line). This calibration constant was found to be 1350 microns/V.

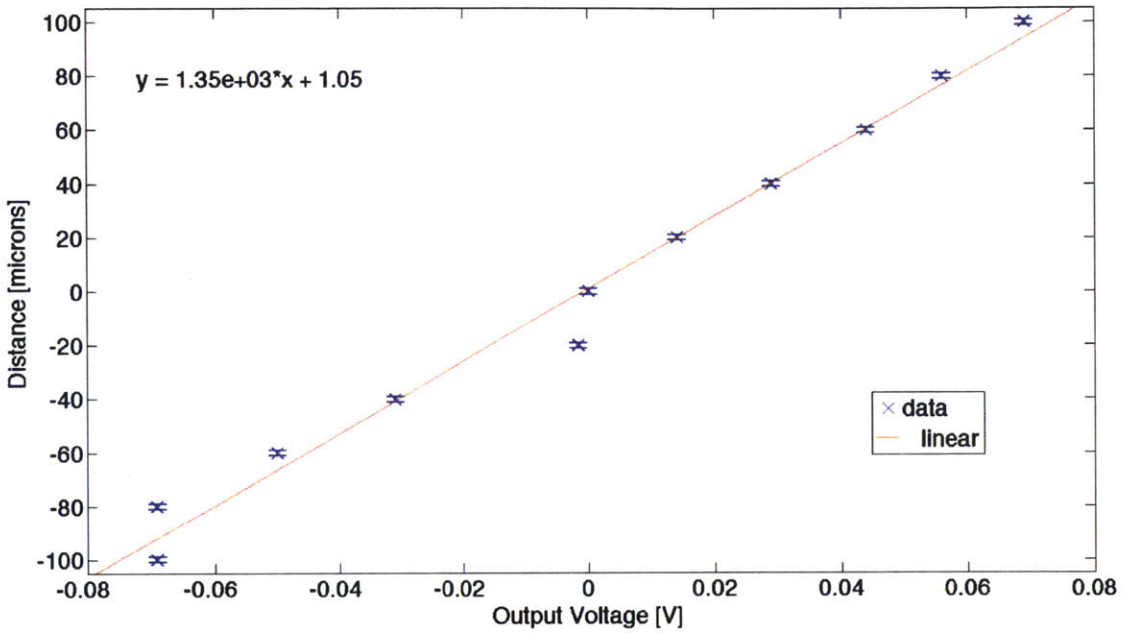

Figure 26: Comparison of Output Voltage to Core Displacement.

To measure frequency response of the system, a dynamic signal analyzer (DSA) on LabView was used. The DSA measures the frequency response of the system by inputting a sinusoidal input at given amplitude and varying frequencies, and comparing it to the output signal measured. The DSA was set to vary the frequency of the input signal from 100*Hz* to 10000*Hz* with amplitude of 10V (corresponding to 1.5 micron displacement), sampling data at sampling rate of 20000*Hz*. A National Instruments myRIO is used to interface the from the signal conditioner to the DSA on LabView. Figure 27, shows the test setup used.

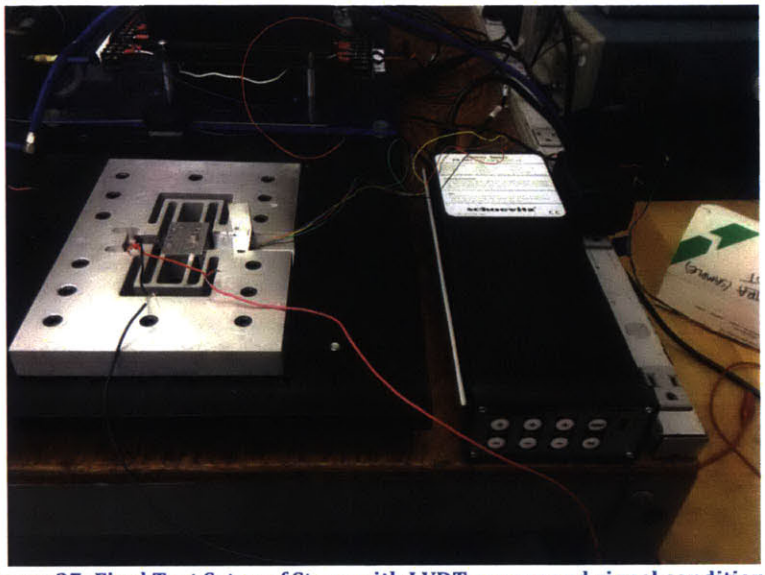

Figure 27: Final Test Setup of Stage with LVDT sensor and signal conditioner

Chapter 6: Results & Discussion

6.1: Experimental Results

The measured frequency response is shown in Figure 28. Comparing the expected frequency response to the measured response, the expected damping of the system is much higher than what is measured. In addition, the system experiences higher order resonances occurring after the first peak that was not modeled in the expected response. Thus, a new model was created to provide to better approximate behavior of the system.

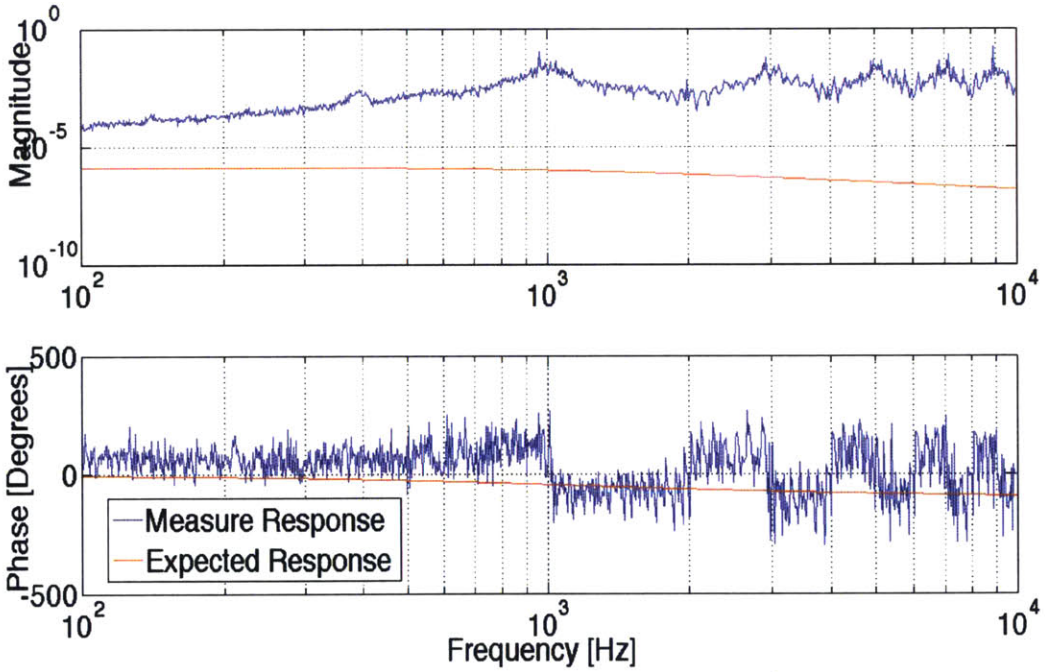

Figure 28:Comparison of Expected Response to Measured Response

To characterize the fitted model, a series of pairs of poles and zeros were placed in series of each. Each pair of pole and zero is defined as follows:

$$G_{pole} = \frac{1}{\left(\frac{1}{\omega_n^2}\right)s^2 + \frac{2\xi}{\omega_n}s + 1} \quad [51]$$

$$G_{zero} = \left(\frac{1}{\omega_n^2}\right)s^2 + \frac{2\xi}{\omega_n}s + 1 \qquad [52]$$

The natural frequencies were determined from the measured frequency response. The damping ratio was iterated until the model fitted the measured response. In addition to these poles and zeros, the +2 slope before the first resonance frequency indicates that two zeros are present at the origin of the s-plane. Finally, a gain of 2.25×10^{-8} is added to align the measured magnitude response to the fitted response. The fitted model is compared to the measured response in Figure 29. The fit provides an approximately good fit to the data. There seems to be some deviation of the fit from the measured response in the phase response. This deviation is caused by the low signal-to-noise ratio created by the small voltage output of the signal conditioner. Because the minimum voltage the myRIO could read was $\sim 1\ mV$, the output voltage of the signal conditioner (ranging $\sim +/- 5mV$) produced a very low signal-to-noise ratio when read by the myRIO.

The transfer function of the model consists of three pairs of zeros and four pairs of poles, and is shown as follows:

$$G_{fit} = \frac{2.25*10^{-8}s^2(2.5*10^{-7}s^2+7.5*10^{-5}s+1)(6.25E10^{-8}s^2+4.5*10^{-5}s+1)(2.77*10^{-8}s^2+3*10^{-5}s+1))}{((1*10^{-6})s^2+0.0001s+1)(1.11*10^{-6}s^2+7.33*10^{-5}s+1)(4*10^{-8}s^2+4*10^{-5}s+1)(2.04*10^{-8}s^2+7.414*10^{-5}s+1)} \qquad [53]$$

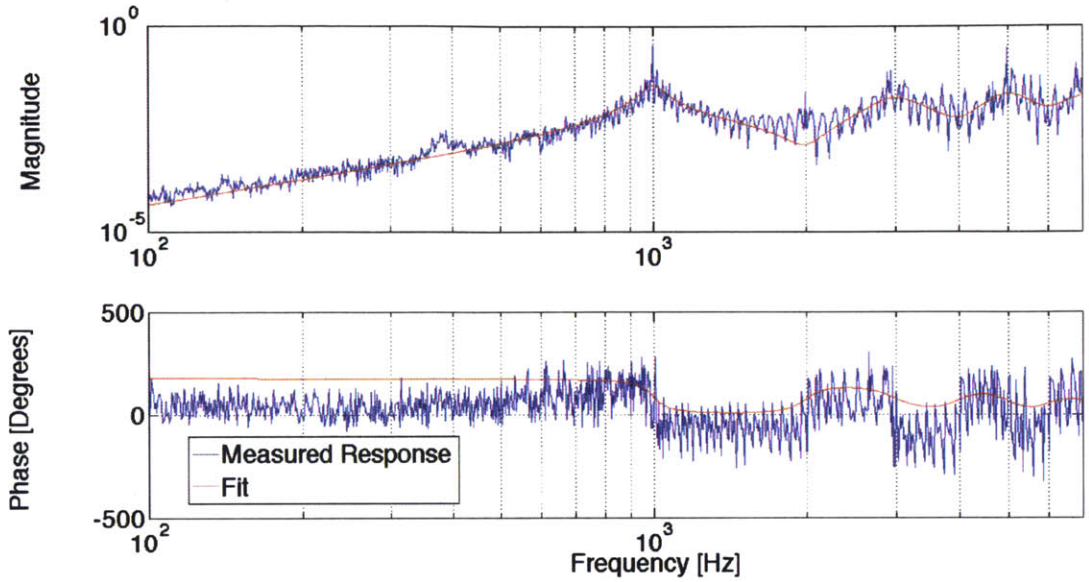

Figure 29: Comparison Fitted Model to Measured Response

Using the fit, an input sinusoidal response is simulated on Matlab. The simulated response has a frequency of 2000*Hz* and amplitude of 10 microns. When introduced, the output response of the system produces a sinusoidal output response with amplitude several of orders of magnitude smaller than the input response. This correlates with the measured response; at a frequency of 2000*Hz*, the magnitude of the system is approximately 1.3×10^{-3}, such a magnitude will drastically reduce the output of the system for any given input. In addition, the system does not reach steady state until ~0.02 seconds, at which the system behaves like the reference signal. The system, however, at this frequency is stable as indicated by the nyquist plot of the loop transmission, shown in Figure 31.

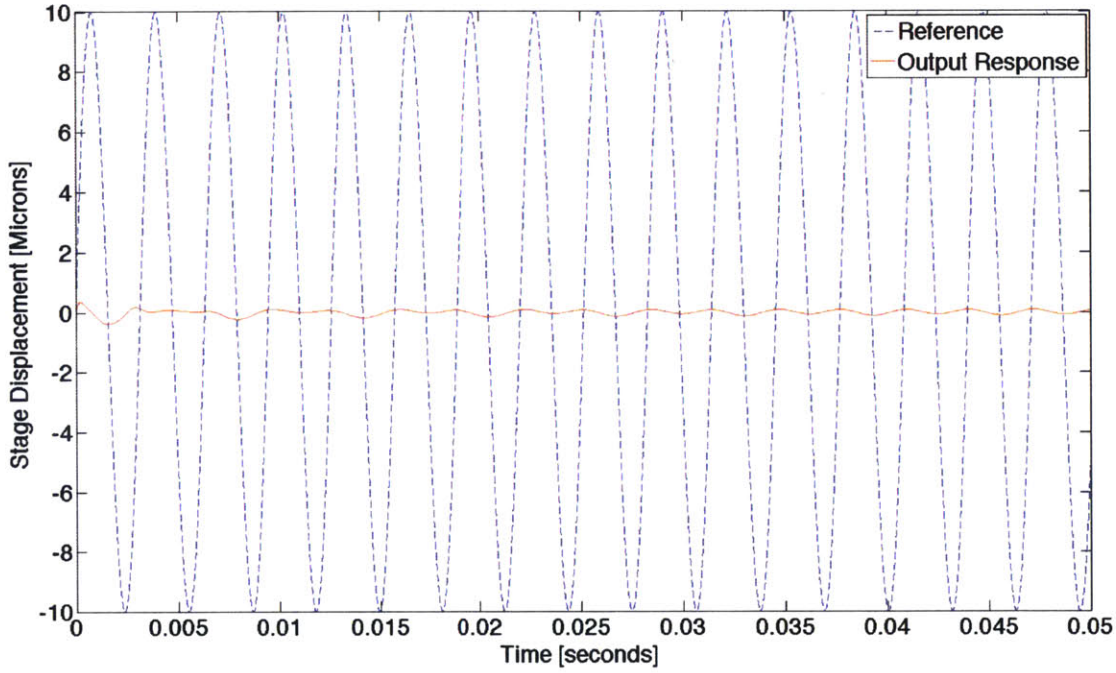

Figure 30: Simulated Input compared against output response of system

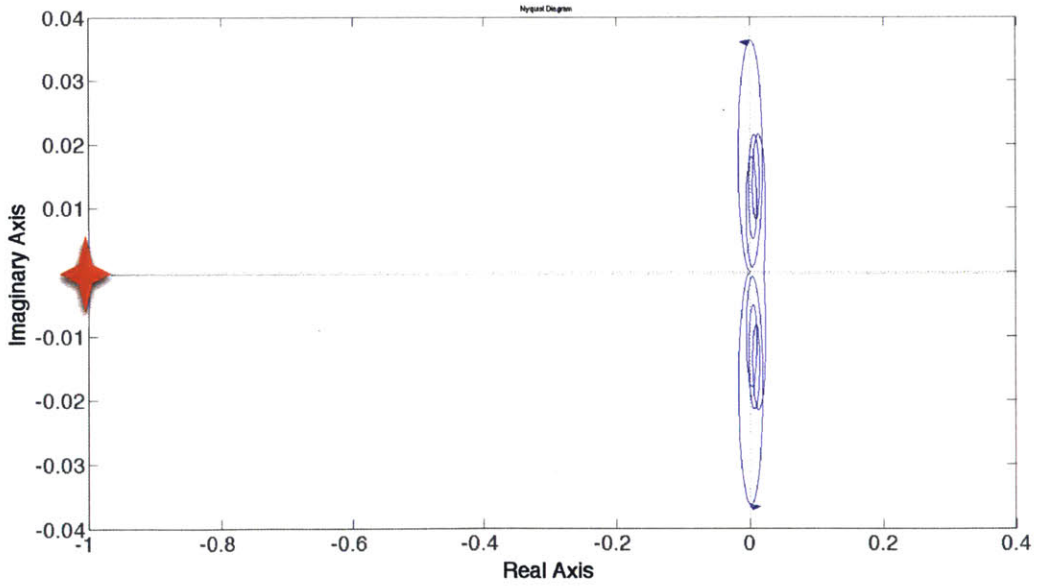

Figure 31: Nyquist plot of fitted model.

For the stage to be used in oscillatory cutting, the system needs a controller that increases the magnitude of the system at the desired driven frequency, while still maintaining a phase margin above zero (> 45 degrees to account for any unforeseen disturbances in the system that might shift operating frequency) and a high enough crossover frequency (at least an order of magnitude higher than $2000Hz$ to ensure that bandwidth of system is sufficiently high enough). It should also be noted that the measured response is very noisy, possibly creating responses in the system that do not exist. To improve on the data, the output of the signal conditioner needs to be amplified to higher voltage to obtain better results from the DSA from LabView. This can be done by means of a more sensitive LVDT or use of capacitance that produces output signals in volts for micron-level displacements.

Chapter 7: Conclusion

A flexural stage was designed with a stiffness of $4.69N/\text{micron}$. The measured frequency response of the system indicates three resonance peaks at $1000Hz$, $3000Hz$, and $5000Hz$. The stage met all of the desired design requirements. A fitted transfer function was shown to provide a good model of the measured frequency response, deviating slightly at higher frequencies. Using the fitted model, a simulated response was introduced and the output response of the system was shown to have the same frequency, but the amplitude was several orders of magnitude smaller. A controller is needed in order to improve the performance of the device.

7.1 Future Work

7.1.1: Characterization of Flexural Stage Design

This research only dealt with measuring the frequency response of a flexural stage that characterized the desired performance for a stage in use in ultramicrotomy. In order to integrate this flexural stage design into ultramicrotomy, a smaller unit must be built and studied. Further characterization of the model's response to external disturbances, must be studied to ensure that stage can perform to desired specifications.

7.1.2: Implementation of a Controller

Given the performance of the system, a controller needs to be designed to improve the performance of the system. Thus, amplification of the output signal from the signal conditioner needs to be implemented in order to provide a more accurate measured response.

Bibliography

[1] Al-Amoudi, A., Studer, D., and Dubochet, J., 2005, "Cutting artefacts and cutting process in vitreous sections for cryo-electron microscopy," J. Struct. Biol., **150**(1), pp. 109–121.

[2] Studer, and Gnaegi, 2000, "Minimal compression of ultrathin sections with use of an oscillating diamond knife," J. Microsc., **197**(1), pp. 94–100.

[3] Gu, H., Zhang, J., Faucher, S., and Zhu, S., 2010, "Controlled chattering?a new 'cutting-edge' technology for nanofabrication," Nanotechnology, **21**(35), p. 355302.

[4] Shaw, M. C., 2005, Metal cutting principles, Oxford University Press, New York.

[5] Atkins, A. G., 2009, The science and engineering of cutting the mechanics and processes of separating, scratching and puncturing biomaterials, metals and non-metals, Butterworth-Heinemann/Elsevier, Amsterdam; Boston.

[6] Thomas, M., 2015, "http://web.mit.edu/mact/www/Blog/Flexures/FlexureIndex.html."

[7] Monti, J., "Boundary Condition Effects On Vibrating Cantilever Beams," MIT.

[8] Gere, J. M., and Goodno, B. J., 2013, Mechanics of materials, Cengage Learning, Stamford, CT.

[9] PI INC., "Piezo Design: Fundamentals of Piezoelectric Actuation."

[10] Hopkins, J. B., and Culpepper, M. L., 2010, "Synthesis of multi-degree of freedom, parallel flexure system concepts via Freedom and Constraint Topology (FACT) – Part I: Principles," Precis. Eng., **34**(2), pp. 259–270.

[11] Piezo Systems, INC, "LOW VOLTAGE PIEZOELECTRIC STACKS."